Unlocking mixed oxides with unprecedented stoichiometries from heterometallic metalorganic frameworks for the catalytic hydrogenation of CO 2

Javier Castells-Gil, Samy Ould-Chikh, Adrian Ramírez, Rafia Ahmad, Gonzalo Prieto, Alberto Rodriguez Gómez, Luis Garzon-Tovar, Selvedin Telalovic, Lingmei Liu, Alessandro Genovese, et al.

Unlocking mixed oxides with unprecedented stoichiometries from heterometallic metalorganic frameworks for the catalytic hydrogenation of CO2

Javier Castells-Gil[a], Samy Ould-Chikh[b], Adrian Ramirez[b], Rafia Ahmad[b], Gonzalo Prieto[c], Alberto Rodriguez Gómez[b], Luis Garzon-Tovar[b], Selvedin Telalovic[b], Lingmei Liu[d], Alessandro Genovese[e], Natalia M. Padial[a], Antonio Aguilar-Tapia[f], Pierre Bordet[f], Luigi Cavallo[b], Carlos Martí-Gastaldo[a]*, Jorge Gascon[b]*

[a] Instituto de Ciencia Molecular (ICMol), Universitat de València, Catedrático José Beltrán, 2, 46980, Paterna (Spain).
[b] King Abdullah University of Science and Technology, KAUST Catalysis Center (KCC), Advanced Functional Materials. Thuwal 23955, Saudi Arabia.
[c] ITQ Instituto de Tecnología Química, Universitat Politècnica de València-Consejo Superior de Investigaciones Científicas (UPV-CSIC), Avenida de los Naranjos s/n, Valencia 46022, Spain
[d] King Abdullah University of Science and Technology, Advanced Membranes and Porous Materials Centre, Thuwal 23955-6900, Saudi Arabia
[e] King Abdullah University of Science and Technology, Core Labs, Thuwal 23955, Saudi Arabia.
[f] Institut Neel, UPR 2940 CNRS – Université Grenoble Alpes, F-38000 Grenoble, France

Abstract

Their complex surface chemistry and high oxygen lattice mobilities place mixed metal oxides among the most important families of materials, with industrial applications from heterogeneous catalysis to sensing and semiconductor industry. Modulation of stoichiometry in mixed metal oxides has been shown as a very powerful tool to further tune optical and catalytic properties. However, accessing different stoichiometries in mixed metal oxides is not always possible through traditional synthetic protocols. Here, we show that, using a bimetallic metal organic framework as precursor it is possible to synthesize mixed metal oxide catalysts with a similar metal to metal stoichiometry as that of the original MOF phase. More specifically, the thermal decomposition of the recently reported MOF MUV-101(Fe, Ti) results in the formation of carbon-supported titanomaghemite nanoparticles with an unprecedented Fe/Ti ratio close to 2, not achievable by soft-chemistry routes. The resulting titanomaghemite phase displays an outstanding catalytic activity for the production of CO from CO_2 via the reverse Water-Gas Shift (RWGS) reaction, with CO selectivity values of *ca.* 100 % and no signs of deactivation after several days of time on stream. Theoretical calculations suggest that the reaction mechanism is promoted by the formation of COOH* species, resulting in the favorable formation of CO over other byproducts like CH_3OH or CH_4. Our work illustrates the exciting possibilities offered by heterometallic MOFs for the production of catalytic materials not accessible through traditional synthetic routes and opens the door to translating the atomic control of metal composition and distribution of the parent MOF onto complex mixed-oxide structures.

Carbon dioxide emissions and their implications for climate change are, most likely, the biggest challenge for our civilization.[1] Yet, the complexity and scale of the issue have so far hampered real progress in the implementation of technological solutions to address this challenge. The lack of progress in the implementation of CO_2 utilization technologies is an outstanding example: for these technologies to become part of the solution and not an additional problem, several factors need to be taken into account: (i) the required energy to transform CO_2 into valuable assets should be 100 % renewable, (ii) the CO_2 footprint of any potential process should be minimum (i.e. by avoiding energy intensive separation processes) and (iii) the potential product(s) should be highly demanded. With these requirements in hand, the transformation of CO_2 to CO is regarded as a key technology. CO is arguably the most important C_1 building block in a variety of industrial processes such as carbonylation of organic compounds,[2] the production longer chain hydrocarbons through the Fischer-Tropsch (FTS) process,[3] the synthesis of methanol and synthetic (CO_2 neutral) fuels[4,5] or the synthesis of important chemicals such as acetic acid.[6] More importantly, CO can be produced from CO_2 and water using renewable energy either via direct electrolysis or in a two-step process involving water electrolysis to produce H_2 followed by the thermocatalyc hydrogenation of CO_2 through the reverse Water-Gas Shift (RWGS) reaction. In spite of important advances in the direct electrocatalytic transformation of CO_2 to CO, the high efficiency of water electrolyzers to produce H_2 and the technological maturity of thermocatalytic processes both point to the two-step process as a very interesting path to follow.

The conversion of CO_2 to CO via reverse water gas shift (RWGS) is endothermic (ΔH^0_{298} = +41,1 kJ mol^{-1}).[7,8] As consequence of the relatively high temperatures required, catalysts deactivation either by sintering or carbon deposition (i.e. cocking) are the most predominant issues. Currently, most of the research on new catalysts for this reaction focuses on precious metals, with non-noble metal catalysts being rare. Among the latter, iron oxides are promising and inexpensive candidates.[9,10] However, the presence of H_2 and CO at high temperatures often results in the formation of metallic iron and iron carbides. The latter phases enable the production of methane and other hydrocarbons, with subsequent cocking and catalyst deactivation.[11] This is why research efforts to stabilize the oxidic form of iron are explored since the century-old Fe_2O_3-Cr_2O_3 catalyst, notable for its use in high temperature water gas shift.[12–14]

An alternative strategy to stabilize the oxidized state of iron is via the formation of a mixed oxide based on the Fe-Ti-O system.[15] Considering the FeO-Fe_2O_3-TiO_2 phase diagram, several candidates are worth being considered: ferrous pseudobrookite ($FeTi_2O_5$), pseudobrookite (Fe_2TiO_5), ilmenite

($FeTiO_3$), and the ulvöspinel (Fe_2TiO_4).[16] F**igure S1** in the supplementary information provides the free energy of reaction for the formation of 1 mol of either Fe or Fe_3C at RWGS thermodynamic equilibrium (P_{eq} = 1 bar, CO_2:H_2 = 1:3). At temperatures higher than 300 °C (*eg.* $\chi_{eq}(CO_2)$ >22 %), the Fe_2TiO_4 spinel is the only one to display a positive free energy for both the formation of Fe_3C and Fe, and consequently stands out as the best potential catalyst. Calculations of the corresponding equilibrium composition of the solid phase show that 78-84 % of iron can be stabilized in its Fe(II) state at 1 bar in the 375-475 °C temperature range (**Figure S2**). Unfortunately, most of the reported syntheses of such materials are solid-state based method, which require prolonged heating at very high temperatures (>1000 ºC) and result in micron sized particles with little to none use in catalytic applications.[17–19] Some reports have claimed the possibility to obtain titanomaghemite nanoparticles (NPs) by soft-chemistry synthetic procedures,[20–24] although Pearce *et. al* have shown the difficulties in incorporating titanium in the spinel structure below a Fe/Ti ratio of ca. 6.5.[24]

With the objective in mind of achieving the manufacture of nano-sized particles of titanomaghemite with a high Ti content, along with the recent discovery of multimetallic MOFs,[30–32] we decided to explore the potential of bimetallic Metal-Organic Frameworks (MOFs) with a pre-defined Fe-Ti ratio as catalyst precursors. The MOF-mediated synthesis[25] has allowed the formation of carbon-based materials with well-defined morphologies, featuring highly dispersed metallic nanoparticles suitable for catalytic and electrocatalytic applications[26,27] as well as supercapacitors[28] or Li-ion batteries.[29] However, to the best of our knowledge, the use of MOFs containing well defined multimetallic units has been very much underexplored.

Targeting, in accordance to our thermodynamic calculations, Fe-Ti ratios in the order of 2, we selected the recently reported MUV-101(Fe, Ti) framework, featuring heterometallic [$TiFe_2(\mu_3\text{-}O)(O_2C)_6$] secondary building units (SBUs).[33,34] To our delight, the controlled decomposition in N_2 of the parent framework results in the formation of titanomaghemite nanoparticles (NPs) with an unprecedented catalytic performance in the RWGS reaction.

Preparation of the parent catalyst precursor

High-yield synthesis of heterometallic MUV-101(Fe, Ti) at a gram-scale was carried out according to the reported methodology.[34] Scanning electron microscopy (SEM) and Transmission electron microscopy (TEM) images show the absence of amorphous solid and the exclusive presence of isolated octahedral monocrystals with a size ranging from 0.2 to 0.5 μm (**Figure 1**). Energy Dispersive X-Ray (EDX)

and elemental analysis both confirm the homogeneous distribution of Ti and Fe across the solid in a Fe/Ti ratio of 2 (**Figure S3, Table S1**). Phase purity was assessed by means of powder X-Ray diffraction (PXRD) and thermogravimetric analysis (TGA) (**Figure S4 and S5**). The ensemble of reflections observed in the XRD pattern are properly assigned to the *Fd-3m* space group (Le Bail refinement, a = 73.496 Å, R_p = 3.1 % - R_{wp} = 4.3 %; **Figure S4**), which is characteristic of the *mtn* topology. Due to their similar atomic form factors, it is not possible to refine the site occupancies of Ti and Fe using a single data set. Nonetheless, the absence of superlattice reflections indicates there is no particular ordering of Ti and Fe cations in the framework. Still, the diffraction cannot exclude the formation of amorphous MO_xH_y clusters (M = Fe or Ti).[38]

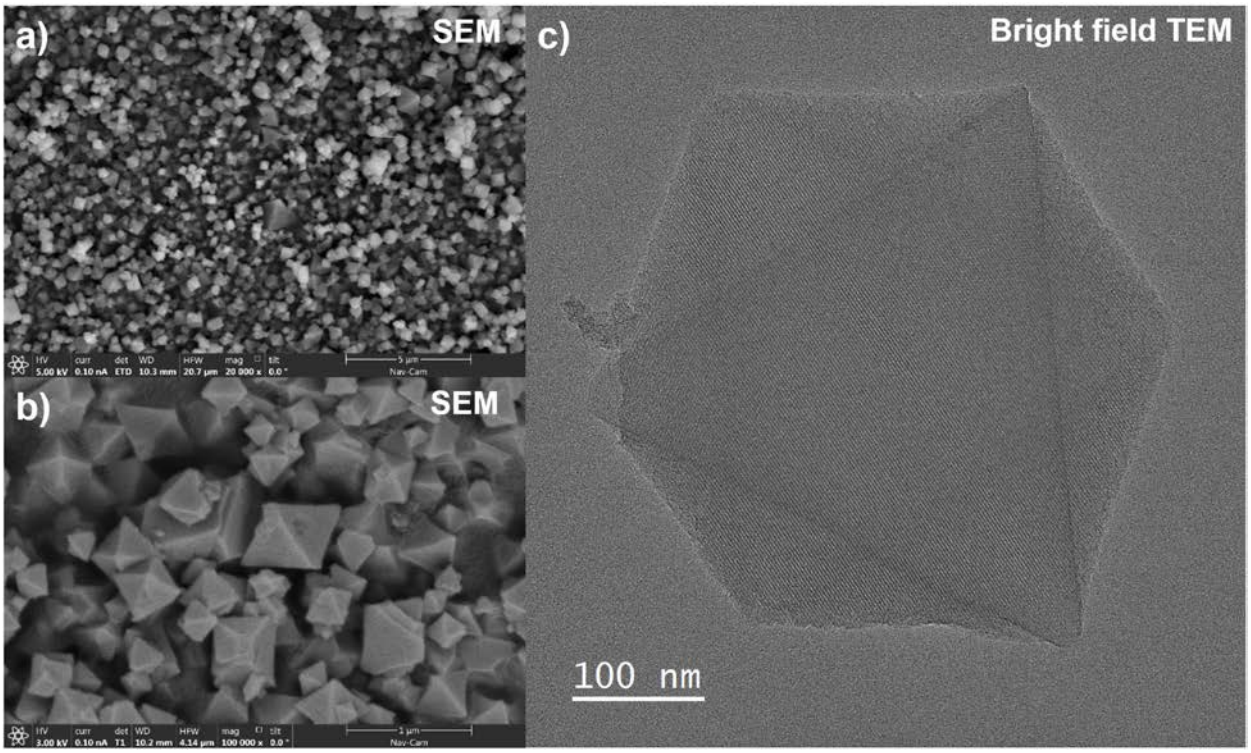

Figure 1. Scanning (a and b) and transmission (c) electron microscopy micrographs of as-made MUV-101(Fe, Ti) crystals.

To discard the formation of amorphous oxides, we carried out a HRTEM study along the <110> crystallographic orientation of the framework. Under this projection, the dodecahedron cages (24 Å) are aligned through two pentagonal apertures, revealing the porous nature of the material (**Figure 2b-c**). In order to visualize the crystal structure of the MUV-101(Fe, Ti) sample, low dose HRTEM was acquired at one vertex of the octahedral crystal along the ⟨110⟩ zone axis using the methodology and the software tools already reported (**Figure 2d**).[39] An electron dose as small as 10 $e^-/Å^2$ preserves the crystal structure since the fast Fourier transform (FFT) of the image display a high lattice fringe resolution of 2.4 Å (**Figure**

2e). The acquired images are not directly interpretable because the phase contrast depends on the interaction of the incident wavefunction along the material thickness and on the contrast transfer function of the objective lens. Nonetheless, both contributions can be calculated quantitatively by multi-slice simulations applied to a well-chosen structural model.[40] Thus, a model MUV-101(Fe, Ti) unit cell was built with a random distribution of titanium and iron cations through the metallic clusters, keeping a 2:1 atomic ratio. Geometrical considerations related to the octahedral morphology provide a sample thickness of 90 nm (**Figure S6a**), which was implemented as a 3x3x12 supercell (>1 million atoms). Defocus (-504 nm) and astigmatism (23 nm) were later determined using the Thon rings that become visible after amorphization of the crystal under high electron dose rate (Figure S6b).[39,41]

The image simulation corresponding to the region of interest (ROI) (**Figures 2**) shows an acceptable agreement between theory and experiment. Further comparison with the projected model of the supercell reveals that the framework appears essentially as a black contrast (**Figure 2h**). Due to the crowded arrangement of the atoms (>10000 atoms per unit cell), only the positions of the supertetrahedra and trimeric clusters surrounding the dodecahedron cages are clearly identified. On the other hand, the porosity of the material is clearly appearing as a homogenous white contrast and further supports the absence of any residual titanium or iron oxide.[42] This is in agreement with the total incorporation of the metal cations in the framework for the formation of an heterometallic [$TiFe_2(\mu_3$-$O)(O_2CR)_6X_3$] cluster in this material as it was elucidated elsewhere by total scattering experiments.[34]

Imaging results are also consistent with the observed type-I+II composite isotherm measured with N_2 physisorption (**Figure S7, Table S1**). The BET and microporous surface area are respectively 2042 and 1871 $m^2.g^{-1}$, in the ballpark of the accessible surface area of 1828 $m^2.g^{-1}$ calculated with the N_2 kinetic diameter (3.314 Å) with the software Zeo++.[43] Two secondary gas uptakes were observed at P/P_0 values of *ca.* 0.05 and 0.13, which are usually ascribed to the filling of the two types of cages found in the MIL-100 structure.[44] The corresponding pore size distribution (PSD) was calculated by the Non-Linear Density Functional Theory (NLDFT) method using various slit and cylindrical shaped pore kernels. All models tested tend to provide lower pore widths compared to the two cage sizes calculated via Monte Carlo simulation (21 Å and 28 Å).[45] Eventually, the most suitable NLDFT kernel is a cylindrical shaped pore model for oxide surfaces displaying the two major pore widths of 19 and 24 Å. The total pore and micropore volume (t-plot) are 0.93 and 0.78 $cm^3.g^{-1}$ respectively, also in close range of the theoretical pore volumes (probe-occupiable: 0.85 $cm^3.g^{-1}$, helium: 0.94 $cm^3.g^{-1}$, geometrical: 1.02 $cm^3.g^{-1}$).[46,47]

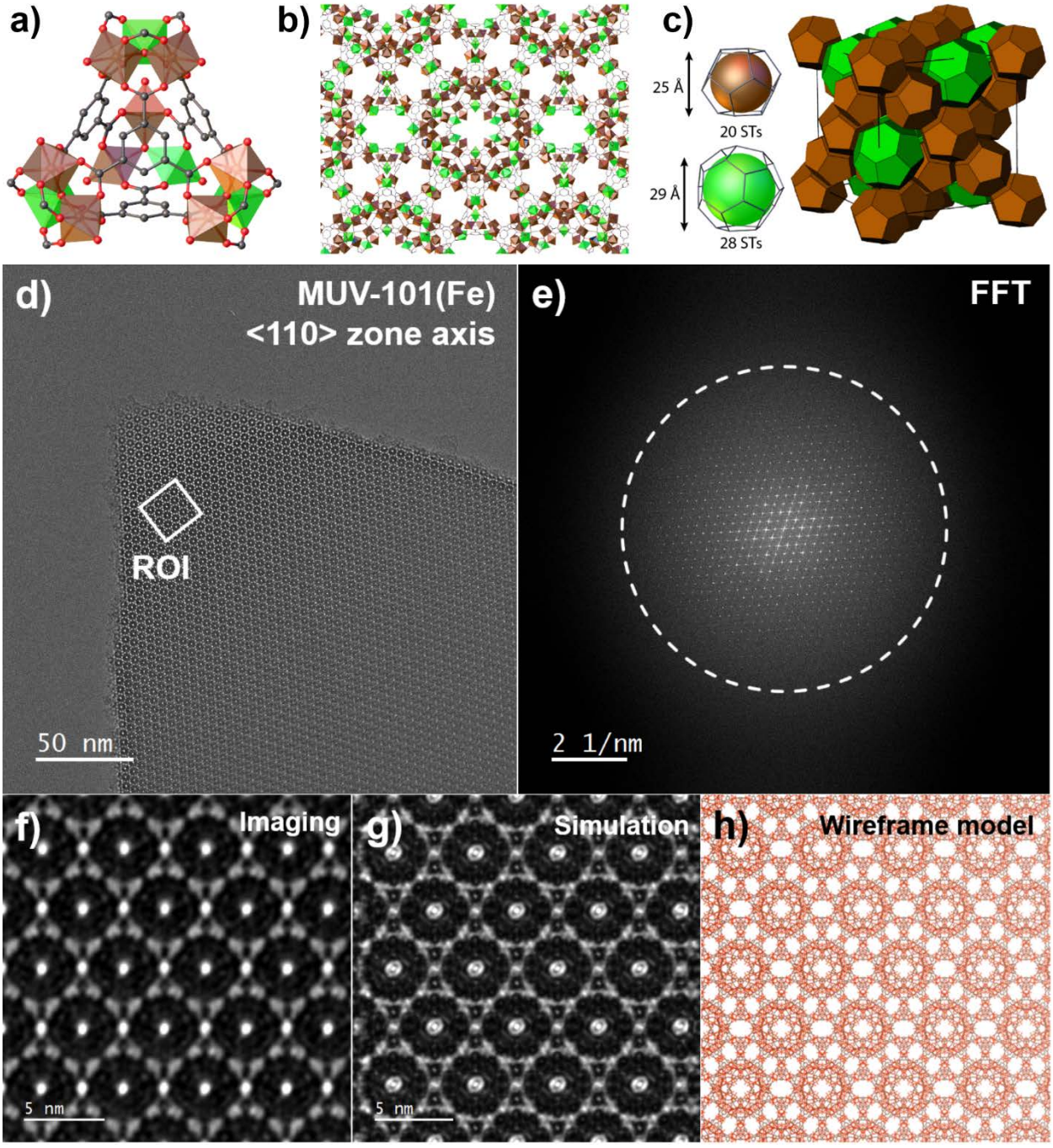

Figure 2. (a) Illustration of a hybrid supertetrahedron (ST) built from trimeric metal octahedra linked together by benzene-1,3,5-tricarboxylate. (b) Schematic illustration of the MIL-100 structure viewed along the <110> crystallographic direction. (c) Topology of the MIL-100 unit cell represented as an arrangement of pentagonal dodecahedron cages (brown color) and hexadecahedron cages (green color). (d) Drift corrected HRTEM image of MUV-101(Fe, Ti) viewed along <110> zone axis. (e) The corresponding fast Fourier transform (FFT) in which the dash circle displays the maximum lattice fringe resolution (2.4 Å). (f) Enlarged area of the highlighted area shown as a white square in (d). This region of interest (ROI) was denoised using successively three filters: an average background subtraction filter (ABSF), a Wiener filter and a band pass filter. (g) Multi-slice HRTEM image simulation (sample thickness = 90 nm, defocus = -504 nm, astigmatism = 23 nm - 51 degrees, spherical aberration = 3 mm). (h) Projected structural model of the MUV-101(Fe, Ti).

MOF Mediated Synthesis of Titanomaghemite Nanoparticles

Following previous reports,[15,35,36] we carried out the controlled pyrolysis of MUV-101(Fe,Ti) to form a bimetallic catalyst, denoted as TiFe/C. The bimetallic TiFe/C solid was then produced by heating the as-synthesized MUV-101(Fe, Ti) in a tubular oven up to 600 °C under inert atmosphere (N_2) for 8 hours. The elemental analysis provided by inductively coupled plasma (ICP) and CHN measurements show a substantial amount of carbon (24.6 wt.%) alongside a high content of Ti and Fe in the solid (15.8 wt. % Ti and 31.0 wt. % Fe), consistent with the atomic Ti:Fe ratio of ~2 in the parent crystals. All the SEM/ADF-STEM micrographs confirm that the resulting solids maintain their octahedral morphology after pyrolysis (**Figure 3a and b, Figure S8-S9**). Lattice fringes appearing on the high-resolution image of an octahedra corner highlight roundish crystallites with a 1-8 nm diameter as individual building block of the aggregates (**Figure 3c**). Further elemental analysis of a similar area recorded by STEM-EELS (**Figure 3d-g**), shows that the nanocrystallites are a mixed Ti-Fe oxide considering the homogenous distribution of Ti, Fe and O atoms (overlap of Ti and Fe maps, Ti and O maps - **Figure 3e and f, Figure S10**). Note also the occurrence of a carbon matrix sitting between the nanoparticles, although its presence lessens in the outer layer of the octahedral aggregate (overlap of Ti and C maps - **Figure 3g**).

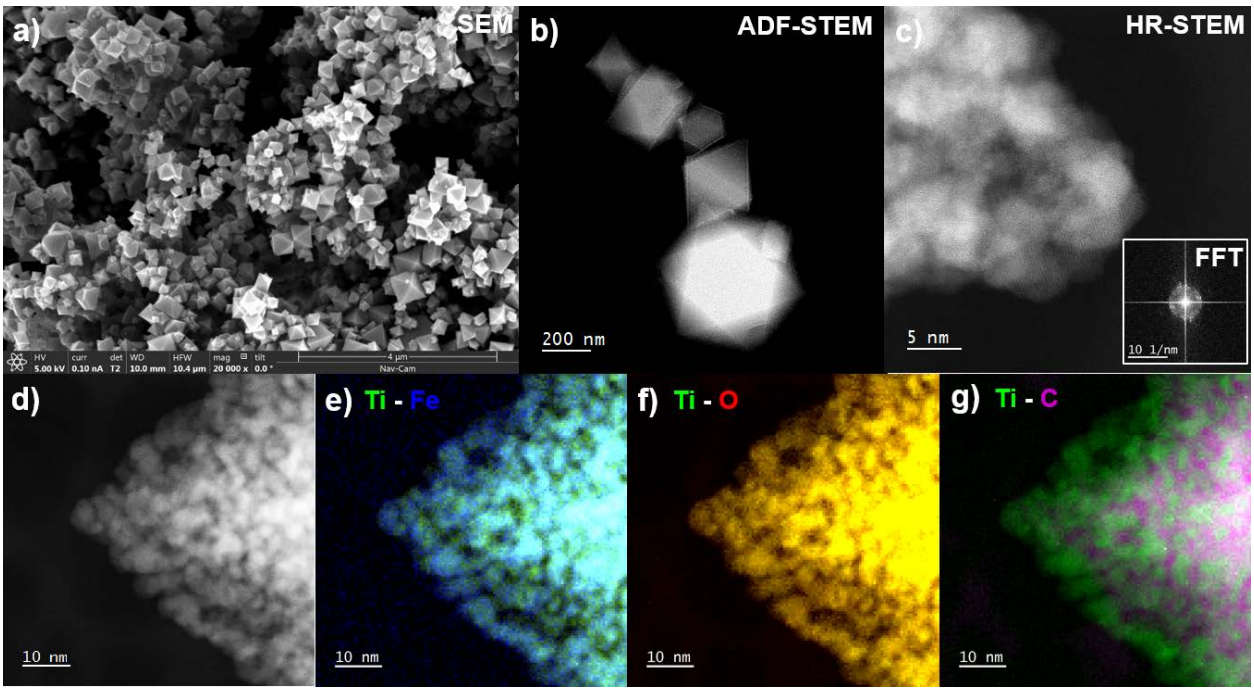

Figure 3. Imaging and chemical mapping of pyrolyzed MUV-101(Fe, Ti) (a) Low magnification SEM micrograph. (b) Low magnification annular dark field STEM micrograph. (c) High-resolution dark field STEM image of an octahedral corner. The inset displays the fast Fourier transform of the same area. (d) A survey image of an octahedral corner used for STEM-EELS characterization: (e) Overlap of the Ti and Fe chemical maps built with Ti and Fe $L_{3,2}$-edges, (f) overlap of the Ti and O chemical maps built with Ti $L_{3,2}$-edge and O K-edge, (g) overlap of the Ti and C chemical maps built with Ti $L_{3,2}$-edge and C K-edge.

The structural changes during the pyrolysis of the MUV-101(Fe,Ti) under N_2 were followed by *in-situ* TEM (**Figure 4, Movie S1**). In a preliminary step (up to 400 °C), the crystals undergo a considerable shrinkage (~20-30 %). Above this temperature, the particles continue to shrink slightly but more importantly, their aspect become granular. This phenomenon corresponds to the bulk formation of small nanoparticles that aggregate along the crystal while maintaining the pseudo-octahedral shape of the original MUV-101(Fe, Ti) crystal. For the biggest crystals (**Figure S11**), the collapse of the MOF ligands is observed as a carbon front moving from the surface to the inside of the aggregates. Most of these events occur in the 400-500 °C range, in agreement with the thermogravimetric analysis performed under N_2 atmosphere (**Figure S12**).

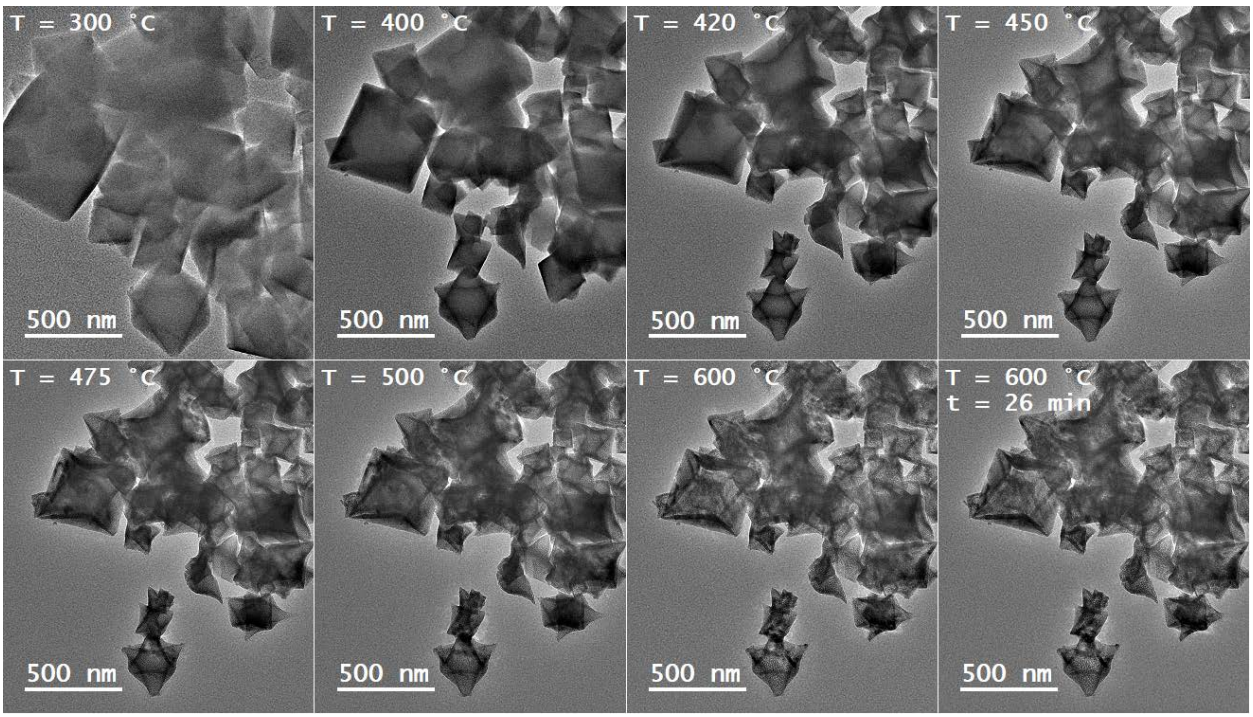

Figure 4. *In-situ* TEM imaging of the MUV-101(Fe, Ti) crystals during pyrolysis from 300 °C up to 600 °C and under 1 bar of N_2. Only selected temperatures are shown. A full movie including images taken at all temperatures during the MOF decomposition is available in supplementary information.

Pyrolysis led also to a complete change of the textural properties as discerned from the composite type-I+II isotherm with a tiny H4-type hysteresis. The BET surface area is reduced from 2042 to 250 $m^2\ g^{-1}$. The microporous volume and surface area as calculated by the t-plot method are 0.07 $cm^3\ g^{-1}$ and 210 $m^2\ g^{-1}$, respectively. This suggests that most of the specific surface area (84%) is located in the microporosity, most probably within the carbon or in-between carbon and oxide nanoparticles. The type of isotherm is characteristic of a material featuring irregularly distributed micro- and mesopores (**Figure S13, Table S1**).[48] The NLDFT results retrieved from a simultaneous treatment of CO_2 and N_2

isotherms are presented in **Figure S13**. These results show that the predominant porosity has a diameter of 5 Å and contributes to ~85% of the total specific surface area in agreement with the former t-plot results. Three minor populations of pores at ~1.2, 3.8 and 35 nm are also observed. The cumulative PSD also shows most of the mesoporous volume (0.08 cm^3 g^{-1}) is broadly distributed over the pores with sizes greater than 2 nm. Those are tentatively assigned to some residual spaces between oxide nanoparticles, *i.e* spaces free from carbon, and intergranular pore between the aggregates.

In order to gain insight into the nanoscale features of the NPs aggregates, such as the nanoparticles size and 3D location, we carried out electron tomography measurements (**Movie S2**). The reconstructed tomograms revealed the existence of two populations of nanoparticles, identified by their higher contrast in the tomographic cross-sections (**Figures 5a and c, Movie S3**). A set of NPs was found decorating the surface of the octahedral particle. They form a uniform, external layer that is embedded with the carbon shell at the surface of the particle. A second set of NPs also shows a uniform distribution but are confined to the empty space offered by the porous carbon matrix. 3D image quantification of the segmented electron tomograms (**Figure5 and d**) was used to analyze specifically the location of both metal dispersions. **Figure 5f** shows the particle size histograms determined for the two populations of metal oxide NPs. The pore-confined set showed a rather narrow size distribution with a number-averaged particle size of 2.2±1.4 nm, whilst the NPs located on the outer surface of the aggregate displayed a number-averaged size of 4.2±1.3 nm. The corresponding surface-averaged nanoparticle sizes were found to be 4.5±2.7 nm and 5.0±1.5 nm, respectively. The analysis also revealed that the fraction of metal confined in the carbon matrix after annealing accounts for >63% of the overall metal oxide surface area, which is ideal to mitigate agglomeration under reaction conditions (*vide infra*). Further analysis of the size of the pore-confined NPs as a function of their 3D Euclidean distance to the geometrical center of the particle analyzed revealed no statistically relevant size gradients. The only statistically significant size differences were found between internal (pore-confined) and external (shell) NPs, suggesting that pore confinement in the carbon matrix is the factor dominating metal oxide clustering upon annealing.

High-resolution X-Ray Photoelectron Spectroscopy (XPS) was applied to the TiFe/C catalyst and the results are shown on **Figures S14-S15** and **Table S3-S4**. The Fe 2p core level spectrum consists of two main broad peaks at 779.8 eV and 794.9 eV corresponding to $2p_{3/2}$, $2p_{1/2}$ spin orbit lines, respectively. The spectrum also contains satellite structures at the high binding energy side of the $2p_{3/2}$ and $2p_{1/2}$ main peaks. To identify the oxidation state of iron, a combined peak fitting of the $2p_{3/2}$-$2p_{1/2}$ region was

conducted.[49–51] The Fe $2p_{3/2}$ spectrum is decomposed with two contributions assigned respectively to the Fe^{3+} core levels and the associated shake-up satellite (711.1 and 719.6 eV), as well as the Fe $2p_{1/2}$ analogues (724.7 and 733.4 eV). There is no detectable presence of Fe(II) in the pyrolysed sample. The Ti $2p_{3/2}$ and $2p_{1/2}$ signal both correspond to the Ti(IV) oxidation state with peak maximum at respective binding energies of ca. 458.3 and 464.2 eV**.** The C 1s core level was fitted using four components located at 284.3 eV, 285.1 eV, 286.7 eV, 289 eV and 289.5 eV corresponding to the C=C(sp^2), C-C/C-H (sp^3), C-O, C=O and O-C=O bonds, respectively.[52,53] The O 1s core level was fitted using three components located at 530.1 eV, 531.7 eV, 533.4 eV corresponding to the M-O-M, M-OH, M-H_2O/C=O bonds, respectively. Although the pyrolyzed sample was protected from air to avoid the re-adsorption of water, the hydroxyl moiety accounts for 19 % of the O 1s surface signal. Besides, accurate quantification of the non-dissociative adsorbed water is hampered by the overlap with the C=O bond peak whose presence was simultaneously observed in the C 1s spectrum.[54]

Experimental powder XRD patterns of the catalyst were acquired with a Mo $K\alpha_1$ radiation which allows the measurement of an extended region of scattering vectors (Q = 17 $Å^{-1}$) and are shown on **Figure 6a** for MUV-101(Fe, Ti), and the TiFe/C catalyst. The MUV-101(Fe, Ti) pattern (**Figure 6a, top trace**) shows sharp Bragg peaks that vanish completely after the pyrolysis step (**Figure 6a, middle trace**). Instead, the XRD pattern for TiFe/C is rather diffuse and shows only a few broad Bragg-like peaks that overlap considerably. In case of the bimetallic TiFe/C solid, the few observable reflections were assigned as a first approximation to the *Fd-3m* space group which is the usual space group for most of the reported spinel structures[55] including the titanomagnetite phases[56] (Le Bail refinement, a = 8.317 Å, R_p = 5.5% - R_{wp} = 7.3%), and alternatively to the *$P4_332$* space group assigned to the titanomaghemite phases (Le Bail refinement, a = 8.322 Å, R_p = 4.2% - R_{wp} = 5.6%) (**Figure S16a**).[57] A very minor presence of large crystallites of ferrite (α-Fe) is noted thanks to the observation of the narrow {110} reflection (from the *bcc* unit cell (Q = 3.11 $Å^{-1}$, 2θ = 20.25 °). Thus, the best match was obtained with the *$P4_332$* space group but the residual remains significant due the diffuse character of the powder diffraction patterns. As result, we could not use conventional Rietveld refinement for determining the atomic structure of the bulk metal oxide formed.

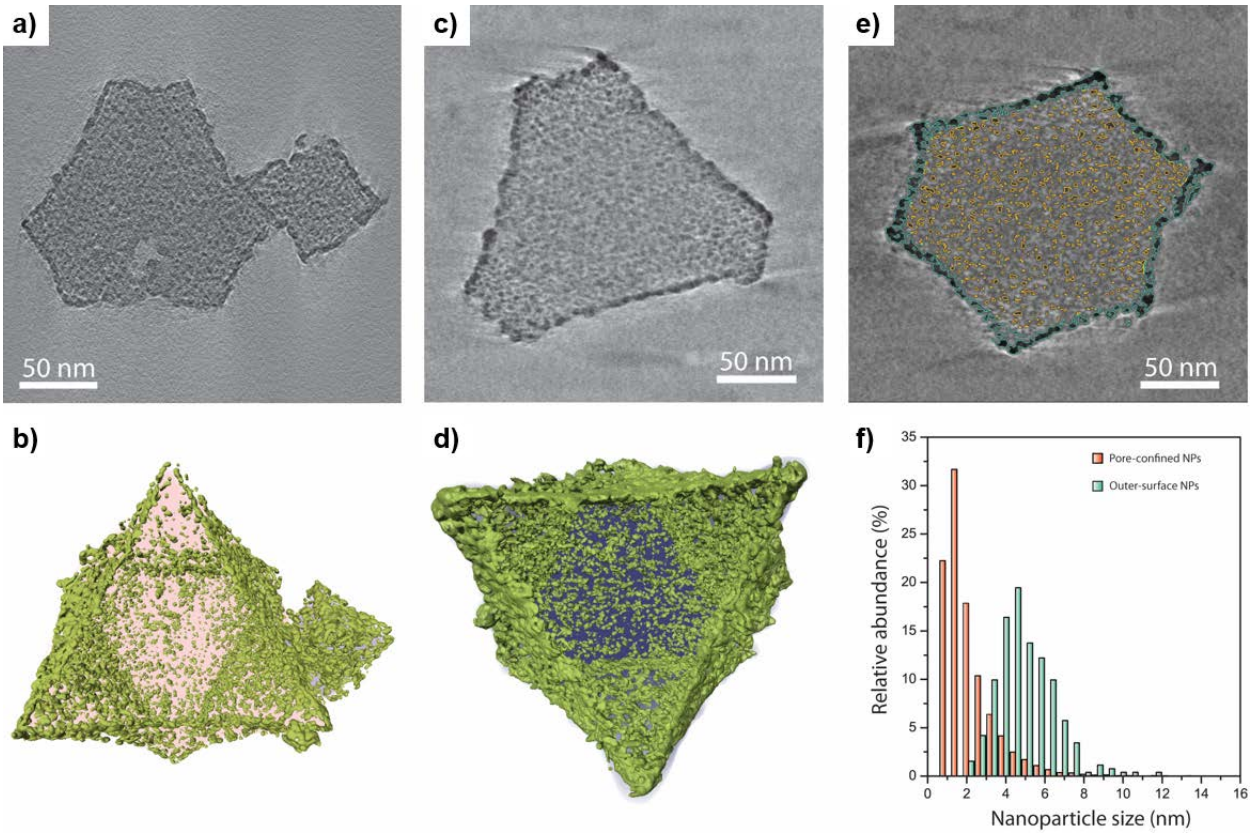

Figure 5: Electron tomography analysis of the TiFe/C catalyst. (a,c) Single voxel-thick mathematical cross sections through the reconstructed tomograms, and **(b,d)** surface-rendered 3D reconstructions of representative catalyst particles as derived from Energy-Filtered Transmission Electron Microscopy (EF-TEM) and Bright-Field Transmission Electron Microscopy (BF-TEM) tomograms. In panels **b** and **d**, metal oxide nanoparticles are depicted in pale green. **(e)** Schematic representation of the location-specific tomogram segmentation results on a selected tomographic slice. Metal oxide nanoparticles confined to the porosity of the carbon matrix are outlined in orange, while those on the outer surface of the carbon-based aggregate particle appear outlined in cyan. **(f)** Location-specific metal nanoparticle size histograms as derived from image analysis of BF-TEM electron tomograms. The two histograms are independent and thus not aggregative.

An alternative strategy is to use the total scattering data that includes both Bragg and diffuse scattering intensities.[58,59] Experimental atomic Pair Distribution Functions (PDFs) are shown in **Figure 6b** with open symbols. All show a series of sharp peaks reflecting the presence of well-defined atomic coordination spheres. The atomic PDF of the MUV-101(Fe, Ti) structure is extremely complex due the large number of atoms in the unit cell (**Figure 6b, top trace**). For a detailed analysis on this that confirms the presence of heterometallic TiFe2 nodes in the framework we refer the reader to a recent contribution.[34] For the pyrolysed MUV-101(Fe, Ti), i.e. TiFe/C, the atomic PDF is markedly different than the parent MOF and decay to zero at a distance of ca. 30 Å, which is shorter than the volume-averaged particle size determined by electron tomography (**Figure 6b, middle trace**). This is usually the sign of a

non-negligible structural disorder, because of finite size and surface relaxation effects often observed with nanoparticles.[60–62]

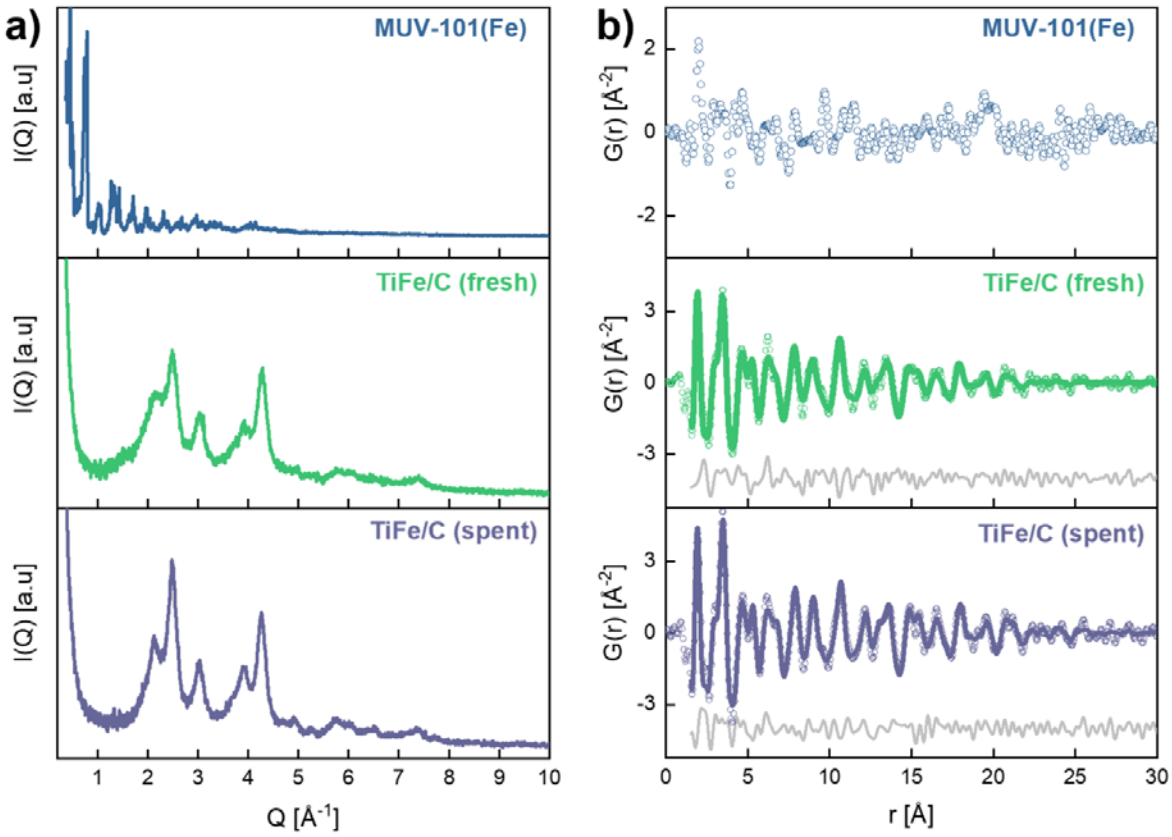

Figure 6. Structural characterization by total scattering experiments of MUV-101(Fe, Ti), TiFe/C catalyst before and after rWGS reaction at 375 °C: (a) experimental diffraction patterns and (b) experimental (open symbols) and cubic-constrained model atomic PDFs (full line). The grey lines are the difference profiles.

Titanomaghemites are non-stochiometric metastable spinels with a general formula:[63]

$$Fe^{3+}_{1-\delta}\,Fe^{2+}_{\delta}[Fe^{3+}_{(2-2x+z+zx)R-1+\delta}Fe^{2+}_{(1+x)(1-z)R-\delta}Ti^{4+}_{xR}\square_{3(1-R)}]O^{2-}_{4},$$

where x is related to the Fe/Ti ratio (Fe/Ti = (3-x)/x), z the fraction of iron atoms oxidized in Fe(III) state, R the spinel stoichiometry parameter (R = 8/[8+z(1+x)]), and δ the number of Fe^{2+} ions on tetrahedral sites. The above equation assumes that both cation vacancies and Ti^{4+} cations are restricted to the octahedral sites. Previous neutron diffraction studies and magnetic measurements have confirmed that Ti^{4+} always occupies the octahedral site both in titanomagnetite and titanomaghemite phases.[64–66] Taking into account elemental analysis (x = 1) and the characterization of metal oxidation state by XPS (z = 1), the structural formula for the present titanomaghemite is expected to be:

$$Fe^{3+}[Fe^{3+}_{0.6}Ti^{4+}_{0.8}\square_{0.6}]O^{2-}_{4}$$

Therefore, the fitting of the experimental PDF for TiFe/C was approached with a traditional crystallography constrained modeling using the primitive cubic lattice of the bulk titanomaghemite spinels (*$P4_332$*) and using the previous structural formula to set the initial values of the metal site occupancies.[57] The fit result in the 1.6 – 30 Å range is shown as a plain line on **figure 6b** (middle trace) and the final values for the refined parameters are all provided in **table S6**. The agreement between the periodic model and the experiment appears reasonable (R_w = 29 %), with a coherent domain of 28 ± 2 Å and with the cubic unit cell dimension of 8.31 ± 0.01 Å. Interestingly, the refinement of the site occupancy factors of both tetrahedral and octahedral sites yielded values way below the original structural formula, with the 4(b) site being completely free of metal cation. Various attempts to enhance the fitting were also performed by adding phases from the Fe-Ti-O thermodynamic diagram (*eg.* Fe, FeO, TiO_2, $FeTiO_3$, Fe_2TiO_5)[16] but resulted only in marginal improvements. Using anisotropic Debye-Waller factors also led to a marginal improvement of the agreement factors in view of the number of parameters introduced. The same was observed when applying a two-phase model where each phase only contained one of the metal elements (**Table S6-S7** and **Figure S16b**).

The presence of metal vacancies was similarly noticed by a recent structural study of γ-Fe_2O_3 nanosized tetrapods solved by PDF analysis.[67] Previous studies have shown that the progressive introduction of titanium in the magnetite (Fe_3O_4), forming titanomagnetites up to the ulvöspinel end-member (Fe_2TiO_4) increases the unit cell parameter from 8.396 Å up to 8.530 Å.[68] On the contrary, the oxidation of magnetite to maghemite requires an exchange of three Fe^{2+} by two Fe^{3+} cations which introduces in the maghemite end-member a total of 2.67 vacancies per unit cell. The overall result is a continuous decrease in the cell parameter from 3.960 Å in magnetite down to 3.340 Å in maghemite.[69] Lastly, Cervellino *et al*. have demonstrated a dependency of the lattice parameter on particle size which follows a D^{-1} law.[70] Consequently, the small unit cell parameter of 8.31 Å, lower than any previous reported values, can be explained both by the absence of Fe^{2+} cations and by the extensive presence of metal vacancies. Maintaining the charge neutrality of such defective nanocrystals requires the presence of hydroxyl groups in the structure. Considering the values of the calculated site occupancy factors, a structural formula can be approximated (assuming the presence of 32 oxygen atoms in the unit cell):

$$Fe^{3+}_{0.55}\square_{0.45}[Fe^{3+}_{0.41}Ti^{4+}_{0.48}\square_{1.11}]O^{2-}_{0.8}(OH)^{-}_{3.2}$$

Solids derived from MIL-100(Fe) alone (labelled as Fe/C catalyst) and a mechanical mixture of MIL-100(Fe) and MIL-100(Ti) (labelled as [Fe+Ti]/C catalyst) were also investigated in order to gain further insight into the importance of starting from a bimetallic MOF. Interestingly, the pyrolysis of

these solids provides respectively a mixture of ferrite (α-Fe) and cementite (Fe_3C) phases and a mixture of hematite (Fe_2O_3) and titania (TiO_2) phases (**Figure S17**). Those results demonstrate clearly that the implementation of two metals in the inorganic node of the MOF precursor enables the formation of mixed oxides not accessible by the pyrolysis of a mixture of homometallic phases. Moreover, our synthesis approach yields small nanocrystals of 5.3 nm (surface-averaged size), which is lower than any former values reported with other synthesis protocols.[20–24]

Catalytic CO_2 Reduction over the Titanomaghemite Catalyst

Initial catalytic tests on the performance of the TiFe/C solid in the CO_2 reduction reaction were carried out at 375 °C, 30 bar, H_2/CO_2 = 3 and a gas hourly space velocity (GHSV) of 12000 $mL \cdot g^{-1} \cdot h^{-1}$. For the sake of comparison, Fe/C and [Fe+Ti]/C catalysts, synthesized respectively from MIL-100(Fe) and a mixture of MIL-100(Ti) and MIL-100(Fe), were also tested. The performance of all catalysts in the hydrogenation of CO_2 after 24 hours is shown in **Figure 7a**. The Fe/C catalyst showed the highest CO_2 conversion (*ca.* 35 %) but a very broad product distribution with low selectivity to CO. Similarly the [Fe+Ti]/C catalyst displayed similar conversion level and product distribution. This is easily understandable as the original Fe_2O_3 phase present in the [Ti+Fe]/C catalyst evolved after reaction towards a mixture of Fe_3C and Fe as in the Fe/C catalyst (**Figure S17**). In contrast, we observed that the TiFe/C catalyst shows a moderate CO_2 conversion of *ca.* 23 % at 375 °C but displays an outstanding high selectivity (*ca.* 96 %) towards the formation of CO.

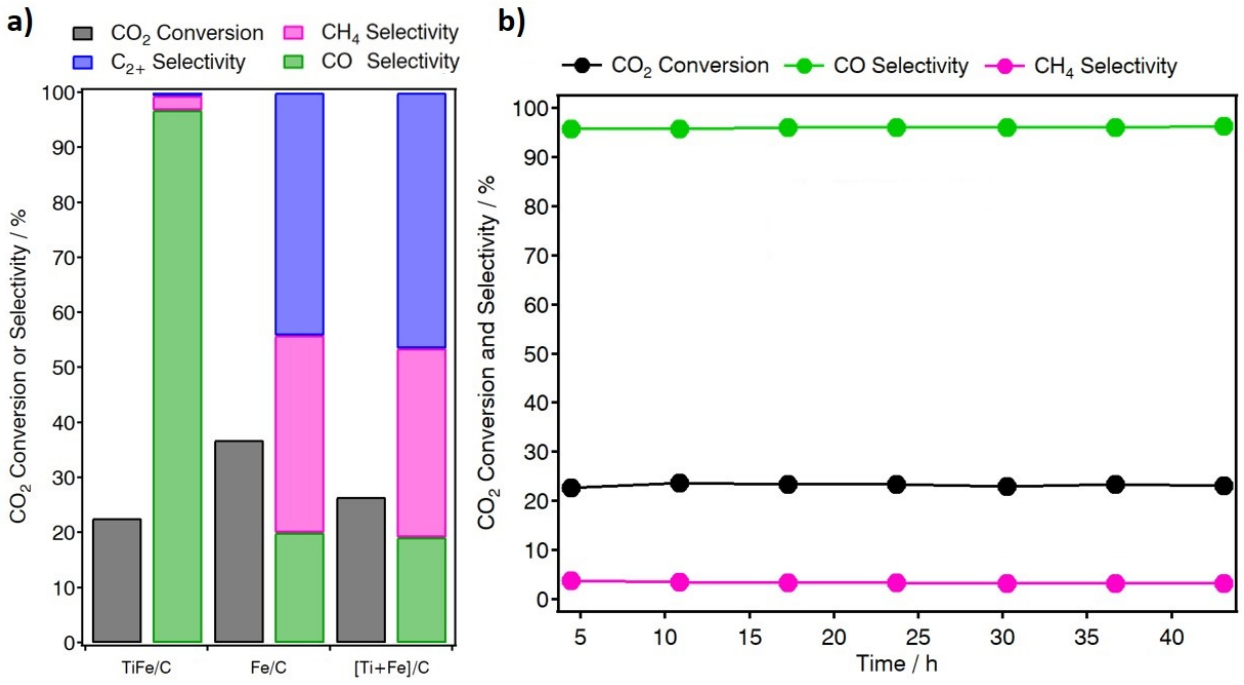

Figure 7. a) CO_2 conversion (black), CO (purple), CH_4 (pink), paraffins (yellow), olefins (blue) and aromatics (red) selectivity values of the hydrogenation of CO_2 over TiFe/C, Fe/C and [Ti + Fe]/C catalysts at 24 hours t.o.s. b) Time evolution of the CO_2 conversion (black) and CO (green) and CH_4 (pink), selectivity values of the hydrogenation of CO_2 over TiFe/C. Reaction conditions: T = 375 ºC, H_2 /CO_2 = 3, P = 30 bar, GHSV = 12000 $mL \cdot g^{-1} \cdot h^{-1}$.

Next, we intended to confirm if the small and defective titanomaghemite nanocrystals obtained by our MOF mediated synthesis possess a unique reactivity compared to Fe-Ti based spinels synthesized by other methods. However, all our attempts to synthesize titanomagnetite nanoparticles via published reverse co-precipitation protocols were unsuccessful (**Table S7**). Although the PXRD patterns of the resulting materials display the characteristic d-spacings of the spinel structure (**Figure S18a**), elemental mapping by STEM-EELS (**Figure S18b**) reveals that Ti atoms are segregated and the nanocrystallites of magnetite are decorated by an amorphous layer of TiO_2 (TiO_2@Fe_3O_4). These results are consistent with a previous report by Pearce *et al.,* who noted that homogeneous nanoparticles were obtained only down to a Fe:Ti ratio of 6.5. At lower ratio, Ti is seggregated in an impurity phase which demonstrate the superiority of our synthesis method to enable the quantitative incorporation of Ti in the spinel structure.[24] Despite metal segregation, TiO_2@Fe_3O_4 catalysts and their oxidation products (TiO_2@γ-Fe_2O_3) were also tested for hydrogenation of CO_2 under the same experimental conditions. None of those precipitated catalysts could reach a CO selectivity as high as the TiFe/C catalyst (34% *vs.* 96%,

Table S8) further supporting that the presence of Ti and its uniform integration in the TiFe oxide are essential to CO selectivity.

The stability of the TiFe/C catalyst was assessed for 48h of RWGS reaction at 375 °C and 30 bar. The conversion and CO selectivity values remained constant during the whole experiment (**Figure S7b**) showing good stability in these reaction conditions. Only few structural changes could be captured after the reaction. STEM images taken after the latter stability test show that the catalyst particles are relatively altered after the reaction (**Figure S19**). For the most part, the modifications are due to the sintering of the nanoparticles on the outer surface of the octahedral agglomerates. Nonetheless, the nanoparticles that are confined inside the porous carbon matrix seems to remain intact. This is remarkable as the titanomaghemite spinels are metastable and reported to invert without change of chemical composition at temperature above 350 °C and at elevated pressure.[71–73] The products resulting from the inversion are usually a multi-phase mixture of TiO_2, $FeTiO_3$, Fe_2TiO_5, Fe_2TiO_4 and α-Fe_2O_3. Furthermore, our initial thermodynamic calculations predicted the formation of Fe_3C and metallic Fe during RWRGS, especially at high pressure (**Figure S2**). Surprisingly, none of those phases were observed after reaction. Indeed, the PXRD pattern of the catalysts recovered after the reaction at 375 °C shows only the titanomaghemite phase (**Figure 6a**, **bottom trace**), although the Bragg peaks are slightly sharper compared to the as-made catalyst. This was treated during the refinement of the PDF by an increase of the coherent domain size up to 33 ± 2 Å and a slight increase of the unit cell parameter up to 8.33 ± 0.02 Å (**Figure 6b, bottom trace**). The rest of the refined parameters remain comparable to the ones calculated for the as-made catalyst (**Table S9**). This further supports the superior chemical stability of the TiFe/C catalyst, compared to other benchmark materials (**Table S10**), where the main changes observed by STEM are mainly due to aggregation of the outer-surface NPs rather than to structural changes during the reaction. Regarding the oxidation state of iron, the fitting of the Fe 2p core level spectrum show the presence of 42 and 58 at.% of Fe(II) and Fe(III) species, respectively on the surface (**Figure S14** and **Table S4**). Since the formation of wüstite (FeO) was not observed, the newly formed Fe(II) cations are assumed to remain in the titanomaghemite nanoparticles. Despite the high hydrogen and the carbon monoxide partial pressure of RWGS reaction, the oxide form of iron can be successfully retained. Thus, the effective integration of Ti in the bimetallic catalyst has a dramatic effect over the stability of the spinel structure under RWGS reaction conditions. The total absence of metallic iron and iron carbide, contrary to previous thermodynamic calculations, suggests that part of the catalyst's stability can be attributed to kinetic stabilization.

Finally, we carried out an optimization of the operating conditions by varying temperature, pressure, contact time and the H_2/CO_2 ratio (**Figures S20-S25**) to push the catalytic performances of the TiFe/C catalyst for the RWGS reaction. See **Table S10** for a summary of our results compared with benchmark materials.[7,8] Compared to the previously reported RWGS catalysts with high CO_2 conversion and high CO selectivity that usually operate at 450 or 600 °C, the TiFe/C catalyst can reach a nearly 100 % selectivity towards the formation of CO as well as higher space time yield (STY) than most of the reported catalysts (even noble-metal based). More importantly, the TiFe/C catalyst is unique regarding its stability, especially challenging at high pressure and temperature.

Density Functional Theory Calculations

We investigated the origin of this unprecedented CO selectivity with density functional theory (DFT) calculations. Our computational models are based on hydroxylated Ti doped Fe_3O_4 surfaces with a Fe:Ti ratio equivalent to 2:1 (Fe_2TiO_4). First, we examined if the most favorable facet of a [111] Fe_2TiO_4 slab is metal or O terminated. Using the protocol detailed in the SI, we evaluated the relative stabilities of the O1, Oct1 and Oct2 terminations of Fe_2TiO_4 [111] surface models in terms of surface energy (σ) as a function of the oxygen partial pressure (**Figure 8a**). In agreement with earlier reports discussing facet terminations at oxygen poor regimes,[74,75] terminations Oct1 and Oct2 have comparable stabilities at temperatures and oxygen partial pressures relevant to the experimental conditions. Termination O1 is less stable than Oct1 and Oct2 by approximately 100 meV/Å^2 (**Figure 8a**). This is also in agreement with earlier reports of magnetite surfaces that suggest the higher stability of ferryl (Fe-O) termination compared to O-terminated surfaces.[76–78] For these reasons, we also considered this facet in further studies relative to the surface termination stabilities. A plot of the dependence on T and p_{O2} of the surface stabilizations in the temperature range of 0-600 °C (**Figure S26**) shows that at every temperature Oct1 (¾ ML of Fe/Ti cations) is the most stable termination for the Fe_2TiO_4 [111] surface.

Next, we followed indications from earlier studies on pure magnetite surfaces suggesting that they are prone to be defective, mostly by metal vacancies.[56,79] We checked the thermodynamics of Fe and Ti vacancy formation on the Oct1 and O vacancy on O1. All the vacancy formation energies we calculated are exothermic (~ -2.5 to -3 eV per unit cell) and tend to stabilize the surface. The most stable vacancy is that of an Fe atom on the Oct1 Fe_2TiO_4 [111] surface.

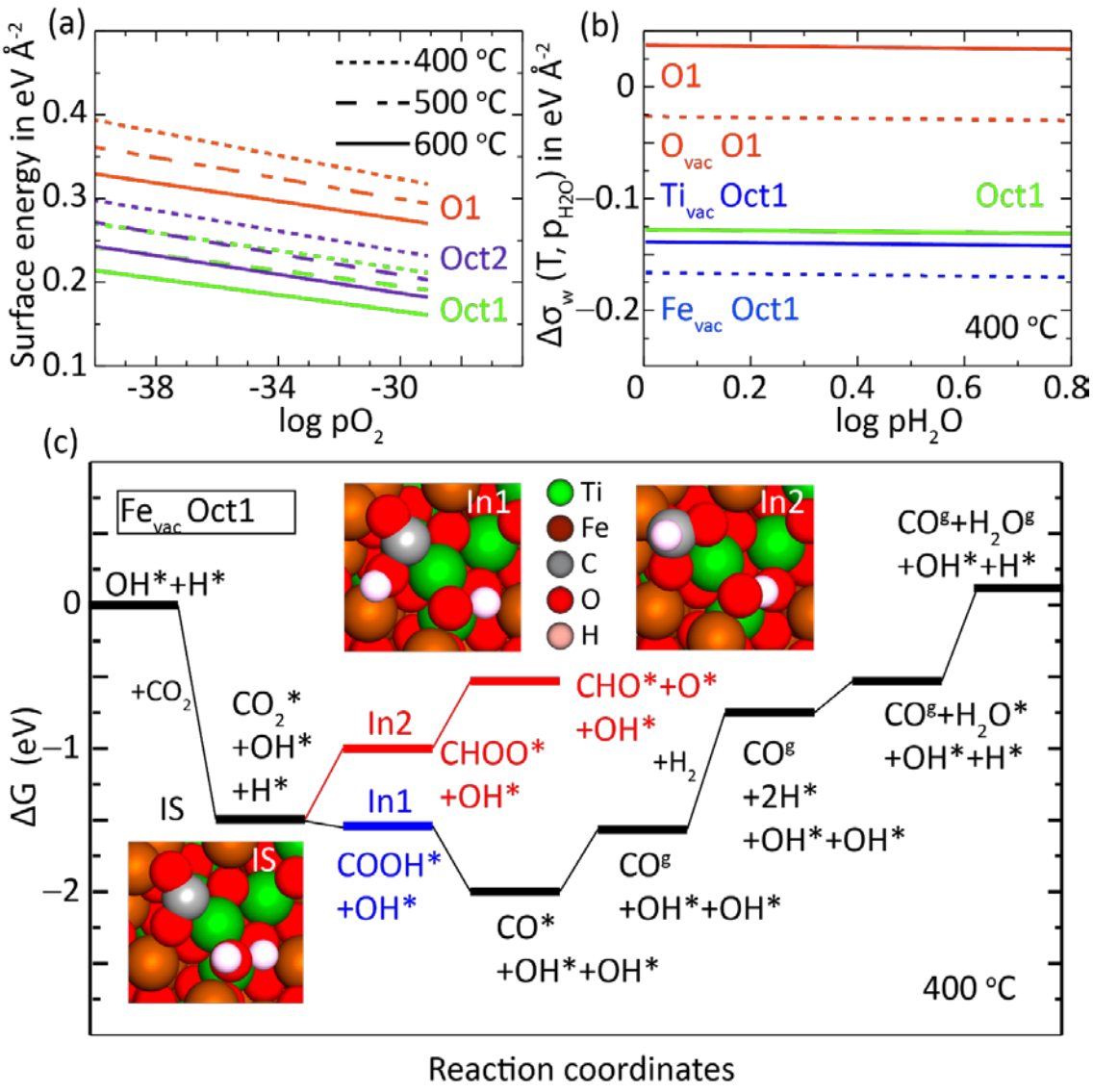

Figure 8. a) PBE + U reported values of surface energies of O1, Oct1, and Oct2 terminations of Fe_2TiO_4 [111] surface at 400, 500 and 600 °C plotted against the chemical potential of oxygen in terms of oxygen partial pressure (p_{O2}). b) Change in surface free energies of hydroxylated O1, O vacancy containing O1, Oct1, Fe vacancy containing Oct1 and Ti vacancy containing Oct1 terminations of Fe_2TiO_4 [111] surface plotted against the water chemical potential in terms of water partial pressure (p_{H2O}) at 400 °C. c) Free energy profile for the reduction of CO_2 on hydroxylated Fe vacancy containing Oct1 termination of Fe_2TiO_4 [111] surface.

As the approximated structural formula of the TiFe/C catalyst suggests a large presence hydroxyl species on the surface of the catalyst, we evaluated how adsorption of a water molecule on these surface terminations affects surface stability. We quantified the effect of water adsorption on the surface stability as the change in surface Gibbs free energy $\Delta\sigma_W(T, p_{H_2O})$ as a function of temperature and water partial pressure[80] (see the SI for a details). One water molecule adsorbed on the simulated Oct1 Fe_2TiO_4 [111] surface stabilizes the surface energy by almost ~0.2 eV/Å^2 (**Figure 8b**). This

stabilization is increased to 0.35 eV/Å^2 in the case a Fe vacancy is present on the Oct1 Fe_2TiO_4 [111] surface, and the adsorbed water molecule dissociates spontaneously at the Fe_{vac} site, forming two OH species, with an overall adsorption free energy of -1.11 eV, at 400 °C. Due to its stability, the hydroxylated Fe_{vac} Oct1 site (**Figure S27**) was selected as model system to investigate the catalytic behavior for the RWGS reaction.

On this hydroxylated Fe_{vac} Oct1 we adsorbed a CO_2 molecule, which binds strongly between Ti and Fe atoms on the surface, via both O and C in a bent like geometry (inset of **Figure 8c**) with highly exothermic adsorption energy (-1.48 eV). We then constructed a free energy pathway (**Figure 8c**) for the CO_2 reduction to uncover the stability of intermediates adsorbed on the active site, leading to high selectivity towards CO. We considered the two relevant reduction pathways for the adsorbed CO_2 molecule: i) the formate pathway, leading to products like methanol and higher hydrocarbons and ii) the carboxyl pathway leading to reverse water gas shift (RWGS) reaction.[81,82] The RWGS pathway can be promoted by formation of the COOH* intermediate, or by the direct dissociation of CO_2* to CO*. The generated COOH* is known to couple with a proton and an electron pair at the active site to obtain CO*. Therefore, the stronger the adsorption of COOH*, the easier it is for COOH* to remain on the surface to participate in the reaction promoting CO* formation.[83] Thermodynamically, formation of COOH* is favored relative to the formation of CHOO*, the former step being exothermic by -0.05 eV, the latter step being endothermic by 0.54 eV (intermediates In1 and In2 in **Figure 8c**). C–O dissociation from In2, leading to CHO* + O*, is also endothermic, by 0.51 eV, ruling out the formate reaction pathway. Along the carboxyl pathway, C–O dissociation from COOH* to CO* and OH* is also exothermic, with an energy gain of 0.44 eV. The easiest sequence of steps leading to release of CO and H_2O starts with desorption of CO, which costs 0.35 eV, followed by dissociative adsorption of a H_2 molecule, endothermic by 0.74 eV, and the catalytic cycle is closed by formation and release of a water molecule.

Alternatively, it should be considered that CO_2 can also react on this hydroxylated surface via a direct dissociation mechanism ($CO_2 \rightarrow CO^* + O^*$) (exothermic by ~0.5 eV). Finally, the plot of **Figure 8c** indicates that hydrogenation of CO* by the surface hydroxyls to CHO* + O* is highly unfavorable and would rather leave the surface as CO(g). We also checked that an added hydrogen molecule, which is spontaneously dissociated as 2H* (endothermic by ~0.3 eV), prefers to form OH* and H* on the surface rather than hydrogenating CO* (**Figure S28**). We can therefore say that the DFT predicted pathway for CO_2 reduction very well coincides with the high CO selectivity observed experimentally.

In summary, our results demonstrate that the use of a bimetallic MOF as catalyst precursor allows the manufacture of mixed oxide materials with stoichiometries not attainable through more traditional synthetic methodologies. The heterometallic nodes in the framework are crucial to warrant the uniform integration of titanium into the titanomaghemite spinel structure while facilitating the stabilization of small and homogenous nanoparticles. The high concentration of surface vacancies in the resulting solids promote the direct hydrogenation of CO_2 to CO through the formation of a COOH* intermediate with unprecedented selectivity. In line with our initial thermodynamic assessment, the obtained titanomaghemite with Fe:Ti ratios close to 2 is stable under reaction conditions, with no sign of deactivation over several hundred hours on stream. These results highlight the unprecedented potential of multimetallic MOFs as precursors for the synthesis of mixed metal oxides not attainable through traditional synthetic routes, with obvious implications not only for catalysis but also in other technological fields, from semiconductor technology to sensing.

METHODS

MUV-101(Fe, Ti) Synthesis: MUV-101(Fe, Ti) was synthesized in a 250 mL Schott glass jar containing trimesic acid dissolved in a mixture of anhydrous DMF (120 mL) and glacial acetic acid (70 mL). The mixture was thoroughly purged with Ar before the addition of $Ti(OiPr)_4$ and anhydrous $FeCl_2$. The clear solution was heated at 120 °C for 48 hours to yield a dark brown microcrystalline solid. The solid was separated by centrifugation and thoroughly washed with fresh DMF and methanol. The solid was further purified by Soxhlet extraction with hot methanol overnight and allowed to dry at room temperature under dynamic vacuum.

Pyrolysis of MUV-101(Fe, Ti): TiFe/C catalyst was synthesized by pyrolysis of the MUV-101(Fe, Ti) in a tubular oven at 600 °C under N_2 atmosphere for 8 hours. After cooling down to room temperature, the pyrolyzed solids were passivated with a stream of 2% O_2 in N_2 at room temperature for 4 hours before being exposed to the ambient atmosphere.

The compositional, textural, and structural properties of the MUV-101(Fe, Ti) precursor and TiFe/C catalyst were investigated by powder X-ray diffraction, pair distribution function analysis, high-resolution transmission electron microscopy, electron energy loss spectroscopy, N_2 and CO_2 physisorption, and X-ray photoelectron spectroscopy. RWGS reaction was performed over undiluted catalysts using a Flowrence® 16 parallel reactor system. Prior to the reaction, the catalyst was preheated

in H_2 at 350 °C and 1 bar for 5 h. Further details on catalyst preparation, characterization, and tests are provided in the Supporting Information.

AUTHOR INFORMATION

* corresponding authors:

Jorge Gascon: jorge.gascon@kaust.edu.sa

Carlos Martí-Gastaldo: carlos.marti@uv.es

Contributions

J.G. and C.M-G. conceived and designed the project. J.C-G. and L.G-T. were responsible for synthesis of the materials. N.M.P. and J.C-G. were responsible for the synthesis and characterization of MUV-101(Fe, Ti). Imaging by transmission electron microscopy, elemental mapping and image simulation were performed by S.O-C. Low-dose HRTEM imaging of MUV-101(Fe, Ti) was performed by S.O-C. assisted by L.L. *In-situ* TEM imaging data were acquired by S.O-C. assisted by A.R. Tomography TEM acquisition and reconstruction was performed by S.O-C. while the related segmentation work was computed by G.P.. A.R.G. and S.T. were responsible for the physisorption measurements. A.R.G. performed the analysis of the XPS data. The PDF data were acquired by S.O-C. and A.A-T. and the following analysis was performed by S.O-C. under the supervision of P.B. All the catalytic tests were performed by A.R. and J.C-G. R.A and L.C performed DFT simulations. J.C-G., A.R., G.P. and S.O-C. drafted the paper. All authors contributed to the writing of the manuscript and gave their approval to the final version.

Competing interests

The authors declare that Universidad de Valencia has applied for a patent on the material MUV-101(Fe, Ti) discussed herein, on which J.C.-G., N.M.P. and C.M.-G. are included as inventors.

Data availability

All data generated and/or analyzed in this study are included in this published article and its supplementary information file and are also available from the corresponding author upon reasonable request.

ACKNOWLEDGMENTS

Daliang Zhang is acknowledged for his help with Digital Micrograph scripts used to acquire image stacks during our *in-situ* TEM experiments. This work was supported by the EU (ERC Stg Chem-fs-MOF 714122)

and Spanish government (CTQ2017-83486-P & CEX2019-000919-M). N.M.P. thanks the European Union for a Marie Skłodowska-Curie Global Fellowship (H2020-MSCA-IF-2016-GF-749359-EnanSET).

References

1. World Meteorological Organization & Atmosphere Watch Global. The State of Greenhouse Gases in the Atmosphere Based on Global Observations through 2016. *World Meteorol. Organ. Bull.* **2015**, 1–4 (2017).

2. Wu, X. F., Neumann, H. & Beller, M. Palladium-catalyzed carbonylative coupling reactions between Ar-X and carbon nucleophiles. *Chem. Soc. Rev.* **40**, 4986–5009 (2011).

3. Dry, M. E. The Fischer-Tropsch process: 1950-2000. *Catal. Today* **71**, 227–241 (2002).

4. Álvarez, A. *et al.* Challenges in the Greener Production of Formates/Formic Acid, Methanol, and DME by Heterogeneously Catalyzed CO2 Hydrogenation Processes. *Chem. Rev.* **117**, 9804–9838 (2017).

5. Wang, W., Wang, S., Ma, X. & Gong, J. Recent advances in catalytic hydrogenation of carbon dioxide. *Chem. Soc. Rev.* **40**, 3703–3727 (2011).

6. Jones, J. H. The Cativa(tm) Process for the Manufacture of Acetic Acid. *Platin. Met. Rev.* **44**, 94–105 (2000).

7. Kattel, S., Liu, P. & Chen, J. G. Tuning Selectivity of CO2 Hydrogenation Reactions at the Metal/Oxide Interface. *J. Am. Chem. Soc.* **139**, 9739–9754 (2017).

8. Nielsen, D. U., Hu, X. M., Daasbjerg, K. & Skrydstrup, T. Chemically and electrochemically catalysed conversion of CO2 to CO with follow-up utilization to value-added chemicals. *Nat. Catal.* **1**, 244–254 (2018).

9. Kim, D. H., Han, S. W., Yoon, H. S. & Kim, Y. D. Reverse water gas shift reaction catalyzed by Fe nanoparticles with high catalytic activity and stability. *J. Ind. Eng. Chem.* **23**, 67–71 (2015).

10. Saeidi, S. *et al.* Mechanisms and kinetics of CO2 hydrogenation to value-added products: A detailed review on current status and future trends. *Renew. Sustain. Energy Rev.* **80**, 1292–1311 (2017).

11. Riedel, T. *et al.* Fischer-Tropsch on iron with H2/CO and H2/CO2 as synthesis gases: The episodes of formation of the Fischer-Tropsch regime and construction of the catalyst. *Top. Catal.* **26**, 41–54 (2003).

12. Bosch, C. & Wild, W. Producing hydrogen. (1913).

13. Keturakis, C. J. *et al.* Dynamics of CrO3-Fe2O3 Catalysts during the High-Temperature Water-Gas Shift Reaction: Molecular Structures and Reactivity. *ACS Catal.* **6**, 4786–4798 (2016).

14. Zhu, M. & Wachs, I. E. Iron-Based Catalysts for the High-Temperature Water-Gas Shift (HT-WGS) Reaction: A Review. *ACS Catalysis* vol. 6 722–732 (2016).

15. Santos, V. P. *et al.* High-temperature Fischer-Tropsch synthesis over FeTi mixed oxide model catalysts: Tailoring activity and stability by varying the Ti/Fe ratio. *Appl. Catal. A Gen.* **533**, 38–48 (2017).

16. TAYLOR, R. W. Liquidus Temperatures in the System FeO—Fe2O3—TiO2. *J. Am. Ceram. Soc.* **46**, 276–279 (1963).

17. Pearce, C. I. *et al.* Fe site occupancy in magnetite-ulvospinel solid solutions: A new approach using X-ray magnetic circular dichroism. *Am. Mineral.* **95**, 425–439 (2010).

18. Lilova, K. I., Pearce, C. I., Gorski, C., Rosso, K. M. & Navrotsky, A. Thermodynamics of the magnetite-ulvöspinel (Fe 3O 4-Fe 2TiO 4) solid solution. *Am. Mineral.* **97**, 1330–1338 (2012).

19. Schoenthal, W. *et al.* Synthesis and magnetic properties of single phase titanomagnetites. in *Journal of Applied Physics* vol. 115 17A934 (American Institute of Physics Inc., 2014).

20. Guigue-Millot, N. *et al.* Chemical heterogeneities in nanometric titanomagnetites prepared by soft chemistry and studied ex situ: Evidence for fe-segregation and oxidation kinetics. *J. Phys. Chem. B* **105**, 7125–7132 (2001).

21. Guigue-Millot, N. *et al.* Control of grain size and morphologies of nanograined ferrites by adaptation of the synthesis route: Mechanosynthesis and soft chemistry. *J. Solid State Chem.* **170**, 30–38 (2003).

22. Yang, S. *et al.* Decolorization of methylene blue by heterogeneous Fenton reaction using Fe3-xTixO4 (0 ≤ x ≤ 0.78) at neutral pH values. *Appl. Catal. B Environ.* **89**, 527–535 (2009).

23. Millot, N., Begin-Colin, S., Perriat, P. & Le Caër, G. Structure, Cation Distribution, and Properties of Nanocrystalline Titanomagnetites Obtained by Mechanosynthesis: Comparison with Soft Chemistry. *J. Solid State Chem.* **139**, 66–78 (1998).

24. Pearce, C. I. *et al.* Synthesis and properties of titanomagnetite (Fe 3-xTi xO 4) nanoparticles: A tunable solid-state Fe(II/III) redox system. *J. Colloid Interface Sci.* **387**, 24–38 (2012).

25. Masoomi, M. Y. & Morsali, A. Applications of metal-organic coordination polymers as precursors for preparation of nano-materials. *Coord. Chem. Rev.* **256**, 2921–2943 (2012).

26. Shen, K., Chen, X., Chen, J. & Li, Y. Development of MOF-Derived Carbon-Based Nanomaterials for Efficient Catalysis. *ACS Catal.* **6**, 5887–5903 (2016).

27. Rodenas, T. *et al.* 2D Metal Organic Framework-Graphitic Carbon Nanocomposites as Precursors for High-Performance O2-Evolution Electrocatalysts. *Adv. Energy Mater.* **8**, 1802404 (2018).

28. Carrasco, J. A. *et al.* Small-pore driven high capacitance in a hierarchical carbon: Via carbonization of Ni-MOF-74 at low temperatures. *Chem. Commun.* **52**, 9141–9144 (2016).

29. Zou, F. *et al.* MOF-derived porous ZnO/ZnFe2O4/C octahedra with hollow interiors for high-rate lithium-ion batteries. *Adv. Mater.* **26**, 6622–6628 (2014).

30. Castillo-Blas, C. & Gándara, F. Metal-organic Frameworks Incorporating Multiple Metal Elements. *Isr. J. Chem.* **58**, 1036–1043 (2018).

31. Abednatanzi, S. *et al.* Mixed-metal metal-organic frameworks. *Chem. Soc. Rev.* **48**, 2535–2565 (2019).

32. Masoomi, M. Y., Morsali, A., Dhakshinamoorthy, A. & Garcia, H. Mixed-Metal MOFs: Unique Opportunities in Metal–Organic Framework (MOF) Functionality and Design. *Angew. Chem. Int. Ed.* **58**, 15188–15205 (2019).

33. M. Padial, N. *et al.* Heterometallic Titanium–Organic Frameworks by Metal-Induced Dynamic Topological Transformations. *J. Am. Chem. Soc.* **142**, 6638–6648.

34. Castells-Gil, J. *et al.* Heterometallic Titanium-Organic Frameworks as Dual-Metal Catalysts for Synergistic Non-buffered Hydrolysis of Nerve Agent Simulants. *Chem* **6**, 3118–3131 (2020).

35. Santos, V. P. *et al.* Metal organic framework-mediated synthesis of highly active and stable Fischer-Tropsch catalysts. *Nat. Commun.* **6**, (2015).

36. Ramirez, A., Gevers, L., Bavykina, A., Ould-Chikh, S. & Gascon, J. Metal Organic Framework-Derived Iron Catalysts for the Direct Hydrogenation of CO2 to Short Chain Olefins. *ACS Catal.* **8**, 9174–9182 (2018).

37. Ramirez, A. *et al.* Tandem Conversion of CO2 to Valuable Hydrocarbons in Highly Concentrated Potassium Iron Catalysts. *ChemCatChem* **11**, 2879–2886 (2019).

38. Castells-Gil, J. *et al.* De novo synthesis of mesoporous photoactive titanium(iv)-organic frameworks with MIL-100 topology. *Chem. Sci.* **10**, 4313–4321 (2019).

39. Zhang, D. *et al.* Atomic-resolution transmission electron microscopy of electron beam–sensitive crystalline materials. *Science* **359**, 675–679 (2018).

40. Koch, C. Determination of Core Structure Periodicity and Point Defect Density Along Dislocations. *PhD Diss.* (2002).

41. Rohou, A. & Grigorieff, N. CTFFIND4: Fast and accurate defocus estimation from electron micrographs. *J. Struct. Biol.* **192**, 216–221 (2015).

42. Jiang, Z. *et al.* Filling metal–organic framework mesopores with TiO2 for CO2 photoreduction. *Nature* **586**, 549–554 (2020).

43. Willems, T. F., Rycroft, C. H., Kazi, M., Meza, J. C. & Haranczyk, M. Algorithms and tools for high-throughput geometry-based analysis of crystalline porous materials. *Microporous Mesoporous Mater.* **149**, 134–141 (2012).

44. Horcajada, P. *et al.* Synthesis and catalytic properties of MIL-100(Fe), an iron(III) carboxylate with large pores. *Chem. Commun.* **100**, 2820–2822 (2007).

45. Pinheiro, M. *et al.* Characterization and comparison of pore landscapes in crystalline porous materials. *J. Mol. Graph. Model.* **44**, 208–219 (2013).

46. Sarkisov, L. & Harrison, A. Computational structure characterisation tools in application to ordered and disordered porous materials. *Mol. Simul.* **37**, 1248–1257 (2011).

47. Ongari, D. *et al.* Accurate characterization of the pore volume in microporous crystalline materials. *Langmuir* **33**, 14529–14538 (2017).

48. Cychosz, K. A., Guillet-Nicolas, R., García-Martínez, J. & Thommes, M. Recent advances in the textural characterization of hierarchically structured nanoporous materials. *Chem. Soc. Rev.* **46**, 389–414 (2017).

49. Fujii, T. *et al.* In situ xps analysis of various iron oxide films grown by (formula presented)-assisted molecular-beam epitaxy. *Phys. Rev. B - Condens. Matter Mater. Phys.* **59**, 3195–3202 (1999).

50. Grosvenor, A. P., Kobe, B. A., Biesinger, M. C. & McIntyre, N. S. Investigation of multiplet splitting

of Fe 2p XPS spectra and bonding in iron compounds. *Surf. Interface Anal.* **36**, 1564–1574 (2004).

51. Aronniemi, M., Sainio, J. & Lahtinen, J. Chemical state quantification of iron and chromium oxides using XPS: The effect of the background subtraction method. *Surf. Sci.* **578**, 108–123 (2005).

52. Zhang, L., Chen, G., Hedhili, M. N., Zhang, H. & Wang, P. Three-dimensional assemblies of graphene prepared by a novel chemical reduction-induced self-assembly method. *Nanoscale* **4**, 7038–7045 (2012).

53. Desimoni, E. & Brunetti, B. X-Ray Photoelectron Spectroscopic Characterization of Chemically Modified Electrodes Used as Chemical Sensors and Biosensors: A Review. *Chemosensors* **3**, 70–117 (2015).

54. Biesinger, M. C. *et al.* Resolving surface chemical states in XPS analysis of first row transition metals, oxides and hydroxides: Cr, Mn, Fe, Co and Ni. *Appl. Surf. Sci.* **257**, 2717–2730 (2011).

55. Blasse, G. Crystal Chemistry and some magnetic properties of mixed metal oxides with spinel structure. *Phillips Res. Reports* **Supplement**, (1964).

56. Wechsler, B. A., Lindsley, D. H. & Prewitt, C. T. CRYSTAL STRUCTURE AND CATION DISTRIBUTION IN TITANOMAGNETITES (Fe3-xTixO4). *Am. Mineral.* **69**, 754–770 (1984).

57. Collyer, S., Grimes, N., Vaughan, D. & Longworth, G. Studies of the crystal structure and crystal chemistry of titanomaghemite. *Am. Mineral.* **73**, 153–160 (1988).

58. Takeshi Egami, Simon J.L. Billinge, S. J. L. B. Underneath the Bragg Peaks Structural Analysis of Complex Materials. (2003).

59. Billinge, S. J. L. & Levin, I. The problem with determining atomic structure at the nanoscale. *Science* vol. 316 561–565 (2007).

60. Gilbert, B., Huang, F., Zhang, H., Waychunas, G. A. & Banfield, J. F. Nanoparticles: Strained and stiff. *Science* **305**, 651–654 (2004).

61. Petkov, V. Nanostructure by high-energy X-ray diffraction. *Materials Today* vol. 11 28–38 (2008).

62. Huang, W. J. *et al.* Coordination-dependent surface atomic contraction in nanocrystals revealed by coherent diffraction. *Nat. Mater.* **7**, 308–313 (2008).

63. Readman, P. W. & O'Reilly, W. Oxidation Processes in Titanomagnetites. *Zeitschrift für Geophys.* **37**, 329–338 (1971).

64. Sato, S., Syono, Y., Ishikawa, Yoshikazu; Sato, S. & Syono, Y. *Neutron and magnetic studies of a single crystal of Fe2TiO4*. *Journal of the Physical Society of Japan* vol. 31 452–460 (1971).

65. O'Reilly, W. & Banerjee, S. K. Cation distribution in titanomagnetites (1-x)Fe3O4 - x Fe2TiO4. *Phys. Lett.* **17**, 237–238 (1965).

66. Stephenson, A. The Temperature Dependent Cation Distribution in Titanomagnetites. *Geophys. J. R. Astron. Soc.* **18**, 199–210 (1969).

67. Petkov, V., Cozzoli, P. D., Buonsanti, R., Cingolani, R. & Ren, Y. Size, shape, and internal atomic ordering of nanocrystals by atomic pair distribution functions: A comparative study of γ-Fe2O 3 nanosized spheres and tetrapods. *J. Am. Chem. Soc.* **131**, 14264–14266 (2009).

68. Lindsley, D. H. Iron-titanium oxides. *Carnegie Inst. Washingt. Yearb.* (1965).

69. Lindsley, D. H. The crystal chemistry and structure of oxide minerals as exemplified by the Fe-Ti oxide. in *Reviews in Mineralogy Volume 3: Oxide minerals (ed. D. Rumble). Mineralogical Society of America* (1976).

70. Cervellino, A., Frison, R., Cernuto, G., Guagliardi, A. & Masciocchi, N. Lattice parameters and site occupancy factors of magnetite-maghemite core-shell nanoparticles. A critical study. *J. Appl. Crystallogr.* **47**, 1755–1761 (2014).

71. Kushiro, I. γ→α Transition in Fe2O3with Pressure. *J. Geomagn. Geoelectr.* **11**, 148–151 (1960).

72. Nagata, T. *Rock Magnetism.* (Maruzen Co. Ltd., 1961).

73. Readman, P. W. & O'Reilly, W. The synthesis and inversion of non-stoichiometric titanomagnetites. *Phys. Earth Planet. Inter.* **4**, 121–128 (1971).

74. Kiejna, A., Ossowski, T. & Pabisiak, T. Surface properties of the clean and Au/Pd covered Fe 3O 4(111): DFT and DFT+U study. *Phys. Rev. B - Condens. Matter Mater. Phys.* **85**, 125414 (2012).

75. Santos-Carballal, D., Roldan, A., Grau-Crespo, R. & de Leeuw, N. H. A DFT study of the structures, stabilities and redox behaviour of the major surfaces of magnetite Fe3O4. *Phys. Chem. Chem. Phys.* **16**, 21082–21097 (2014).

76. Noh, J., Osman, O. I., Aziz, S. G., Winget, P. & Brédas, J. L. Magnetite Fe3O4 (111) Surfaces: Impact of Defects on Structure, Stability, and Electronic Properties. *Chem. Mater.* **27**, 5856–5867 (2015).

77. Yu, X., Huo, C. F., Li, Y. W., Wang, J. & Jiao, H. Fe 3O 4 surface electronic structures and stability from GGA + U. *Surf. Sci.* **606**, 872–879 (2012).

78. Berdunov, N., Murphy, S., Mariotto, G. & Shvets, I. V. Atomically resolved spin-dependent tunneling on the oxygen-terminated Fe3O4(111). *Phys. Rev. Lett.* **93**, (2004).

79. Yuan, K. *et al.* Oxidation induced strain and defects in magnetite crystals. *Nat. Commun.* **10**, 1–10 (2019).

80. Grillo, M. E., Finnis, M. W. & Ranke, W. Surface structure and water adsorption on Fe3 O4 (111): Spin-density functional theory and on-site Coulomb interactions. *Phys. Rev. B - Condens. Matter Mater. Phys.* **77**, (2008).

81. Polo-Garzon, F. *et al.* Elucidation of the Reaction Mechanism for High-Temperature Water Gas Shift over an Industrial-Type Copper-Chromium-Iron Oxide Catalyst. *J. Am. Chem. Soc.* **141**, 7990–7999 (2019).

82. Wang, G. C. & Nakamura, J. Structure sensitivity for forward and reverse water-gas shift reactions on copper surfaces: A DFT study. *J. Phys. Chem. Lett.* **1**, 3053–3057 (2010).

83. Zhang, Q. & Guo, L. Mechanism of the Reverse Water–Gas Shift Reaction Catalyzed by Cu12TM Bimetallic Nanocluster: A Density Functional Theory Study. *J. Clust. Sci.* **29**, 867–877 (2018).